



HAL
open science

Seismoelectric Signals Produced by Mesoscopic Heterogeneities: Spectroscopic Analysis of Fractured Media

Marina Rosas-Carbajal, Damien Jougnot, J Germán Rubino, Leonardo Monachesi, Niklas Linde, Klaus Holliger

► **To cite this version:**

Marina Rosas-Carbajal, Damien Jougnot, J Germán Rubino, Leonardo Monachesi, Niklas Linde, et al.. Seismoelectric Signals Produced by Mesoscopic Heterogeneities: Spectroscopic Analysis of Fractured Media. Seismoelectric Exploration: Theory, Experiments, and Applications, 1, Wiley, 2020, Geophysical Monograph Series, 9781119127376. 10.1002/9781119127383.ch19 . insu-03454768

HAL Id: insu-03454768

<https://insu.hal.science/insu-03454768>

Submitted on 25 Nov 2022

HAL is a multi-disciplinary open access archive for the deposit and dissemination of scientific research documents, whether they are published or not. The documents may come from teaching and research institutions in France or abroad, or from public or private research centers.

L'archive ouverte pluridisciplinaire **HAL**, est destinée au dépôt et à la diffusion de documents scientifiques de niveau recherche, publiés ou non, émanant des établissements d'enseignement et de recherche français ou étrangers, des laboratoires publics ou privés.

1 **Seismoelectric signals produced by mesoscopic heterogeneities:**
2 **spectroscopic analysis of fractured media**

3 **M. Rosas-Carbajal**¹, **D. Jougnot**², **J. G. Rubino**³, **L. Monachesi**⁴, **N. Linde**⁵, **K. Holliger**⁵

4 ¹Institut de Physique du Globe de Paris, Sorbonne Paris Cité, CNRS UMR 7154, Université Paris Diderot, Paris, France

5 ²Sorbonne Universités, UPMC Université Paris 06, CNRS, EPHE, UMR 7619 METIS, Paris, France

6 ³CONICET, Centro Atómico Bariloche - CNEA, San Carlos de Bariloche, Argentina

7 ⁴CONICET, Instituto de Investigación en Paleobiología y Geología, Universidad Nacional de Río Negro, Argentina

8 ⁵Applied and Environmental Geophysics Group, Institute of Earth Sciences, University of Lausanne, Lausanne,

9 Switzerland

10 **Key Points:**

- 11 • Mesoscopic compressibility contrasts cause wave-induced fluid flow
12 • Measurable seismoelectric signals are generated by wave-induced fluid flow
13 • Energy-based approach to study the seismoelectric conversion in fracture networks

Corresponding author: M. Rosas-Carbajal, rosas@ipgp.fr

Abstract

In fluid-saturated porous rocks, the presence of mesoscopic heterogeneities such as, for example, fractures, can produce measurable seismoelectric signals. The conversion of mechanical energy into electromagnetic energy is related to wave-induced fluid flow (WIFF) between the heterogeneities and the embedding background. This physical mechanism is a well-known cause of seismic attenuation, which exhibits a strong frequency dependence related to rock physical and structural properties. Consequently, seismoelectric signals arising from WIFF are also expected to depend on various material properties, such as the background permeability and fracture characteristics. We present analytical and numerical approaches to study the effects of mesoscopic heterogeneities on seismoelectric signals. We develop an energy-based approach to quantify the total energy converted to seismoelectric signals at the sample scale. In particular, we apply our theoretical framework to synthetic models of fractured rock samples and study the spectral signature of the resulting seismoelectric signals. This study highlights the influence of the mechanical and hydraulic properties, as well as the geometrical characteristics, such as degree of fracture connectivity, of the probed medium on the resulting seismoelectric signal.

1 Introduction

One common assumption in seismoelectric studies is that the involved media are homogeneous at the sub-wavelength scale. However, most geological environments typically contain mesoscopic heterogeneities, that is, heterogeneities larger than the pore size but smaller than the dominant seismic wavelength. In presence of contrasts in elastic compliance, the stress field associated with a propagating seismic wave produces a pore fluid pressure gradient and, consequently, wave-induced fluid flow (WIFF), which results in energy dissipation due to viscous friction. Indeed, WIFF is currently considered to be one of the major causes of seismic wave attenuation in the upper part of the Earth's crust [e.g. Müller *et al.*, 2010]. For this reason, efforts directed towards a better understanding of WIFF involving theoretical analyses [e.g., Müller and Gurevich, 2005], laboratory measurements [e.g., Batzle *et al.*, 2006; Tisato and Madonna, 2012; Subramaniyan *et al.*, 2014], and numerical simulations [e.g., Masson and Pride, 2007; Rubino *et al.*, 2009; Solazzi *et al.*, 2016] have been increasing during the last decades. WIFF is a frequency-dependent physical process that is mainly controlled by the permeability, the compressibility contrasts between the heterogeneities and the embedding background, and the geometrical characteristics of the heterogeneities. These properties are of significant relevance for flow and transport modeling, especially in fractured media [e.g. Berkowitz, 2002] and hence the analysis of the impact of WIFF on seismoelectric signals is of broad interest.

Despite its potential importance, only few studies have focused on the understanding of seismoelectric signals due to mesoscopic heterogeneities. In their pioneering numerical work, Haartsen and Pride [1997] mention a significant signal enhancement when considering a thin bed between two half-spaces, but no results or corresponding detailed physical explanations are presented. Similarly, Haines and Pride [2006] showed that layers that are up to 20 times thinner than the seismic wavelength could be detected by the seismoelectric method. More recently, Grobbe and Slob [2016] used numerical simulations to explore the enhancement of the interface response in the contact of two half-spaces when thin beds are located in between these half-spaces (Cite Grobbe and Slob in this book). Although they study constructive and destructive interference resulting from different separations and thicknesses of thin beds, they do not focus on the physical phenomena taking place in the thin bed itself.

A likely explanation why mesoscopic effects on the seismoelectric signal have so far been largely ignored in the scientific literature is high computational cost of corresponding numerical simulations. This cost is due to the fact that the dominant scales at which WIFF takes place, as characterized by the corresponding diffusion lengths, are much smaller than the prevailing seismic wavelengths. Recently, Jougnot *et al.* [2013] presented a new approach for studying the seismoelectric response of mesoscopic heterogeneities that circumvents this limitation. In-

65 instead of performing numerical simulations of wave propagation, they simulated the seismo-
66 electric response of oscillatory compressibility tests on synthetic samples at different frequen-
67 cies. Since the size of the probed sample can be much smaller than the seismic wavelengths,
68 this approach avoids the inherent problems related to the large contrasts in spatial scale be-
69 tween seismic wavelengths and diffusion lengths. The work by *Jougnot et al.* [2013] thus opens
70 an avenue for detailed analyses of seismoelectric responses to mesoscopic heterogeneities. Here,
71 we extend and complement this study. We first describe the underlying theoretical framework
72 used to compute the seismoelectric response of an heterogeneous sample subjected to an os-
73 cillatory compressibility test. Next, we present an energy-based approach to characterize the
74 seismoelectric response at the sample scale, as a substitute to relying on a certain experimen-
75 tal setup, such as, for example, a particular electrode configuration. In order to gain insights
76 into the physical processes that contribute to the seismoelectric response in the presence of
77 mesoscopic heterogeneities, we proceed to explore an analytical solution for a rock sample con-
78 taining a horizontal layer centered in an otherwise homogeneous rock in an initial case and
79 containing a fracture in a second analysis. We then perform a numerical sensitivity analysis
80 of the seismoelectric signals generated in 2D fractured media. For different fracture proper-
81 ties, we present the dependence on frequency and space of the electrical potential amplitude,
82 as well as the frequency-dependent total energy converted to seismoelectric signal in an os-
83 cillation cycle.

84 2 Theory

85 To explore the seismoelectric signals produced by mesoscopic heterogeneities, we em-
86 ploy the methodology proposed by *Jougnot et al.* [2013]. We consider a 2D, fluid-saturated,
87 heterogeneous porous rock sample and study its seismoelectric response to an oscillatory com-
88 pression (Fig. 1). The mechanical response of the probed sample is obtained by solving Biot's
89 (1941) quasi-static equations in the space-frequency domain with adequate boundary condi-
90 tions. The resulting fluid velocity field is then used to calculate the seismoelectric response
91 of the sample. That is, we decouple the seismic and electrical problems [e.g., *Haines and Pride*,
92 2006; *Jardani et al.*, 2010; *Zyserman et al.*, 2010]. In the following, we present the details of
93 the proposed methodology. It is important to mention here that the extension of this approach
94 to 3D is conceptually straightforward, but computationally cumbersome.

95 2.1 Mechanical response

96 Let $\Omega = (0, L_x) \times (0, L_y)$ be a domain that represents the probed 2D sample and Γ
97 its boundary given by

$$98 \quad \Gamma = \Gamma^L \cup \Gamma^B \cup \Gamma^R \cup \Gamma^T, \quad (1)$$

99 where the subscripts $L, R, B,$ and T stand for left, right, bottom, and top boundary, respec-
100 tively,

$$101 \quad \Gamma^L = \{(x, y) \in \Omega : x = 0\}, \quad (2)$$

$$102 \quad \Gamma^R = \{(x, y) \in \Omega : x = L_x\}, \quad (3)$$

$$103 \quad \Gamma^B = \{(x, y) \in \Omega : y = 0\}, \quad (4)$$

$$104 \quad \Gamma^T = \{(x, y) \in \Omega : y = L_y\}. \quad (5)$$

105 We apply a time-harmonic normal compression at the top boundary of the sample. The
106 solid is neither allowed to move on the bottom boundary nor to have horizontal displacements
107 on the lateral boundaries. No tangential forces are applied on the lateral boundaries, and the
108 pore fluid is not allowed to flow into or out of the sample. Thus, the following boundary con-

109 ditions are imposed

$$110 \quad \boldsymbol{\tau} \cdot \boldsymbol{\nu} = (0, -\Delta P), \quad (x, y) \in \Gamma^T, \quad (6)$$

$$111 \quad \mathbf{u} = \mathbf{0}, \quad (x, y) \in \Gamma^B, \quad (7)$$

$$112 \quad (\boldsymbol{\tau} \cdot \boldsymbol{\nu}) \cdot \boldsymbol{\chi} = 0, \quad (x, y) \in \Gamma^L \cup \Gamma^R, \quad (8)$$

$$113 \quad \mathbf{u} \cdot \boldsymbol{\nu} = 0, \quad (x, y) \in \Gamma^L \cup \Gamma^R, \quad (9)$$

$$114 \quad \mathbf{w} \cdot \boldsymbol{\nu} = 0, \quad (x, y) \in \Gamma, \quad (10)$$

115 where $\boldsymbol{\nu}$ denotes the unit outer normal on Γ and $\boldsymbol{\chi}$ is a unit tangent so that $\{\boldsymbol{\nu}, \boldsymbol{\chi}\}$ is an or-
 116 thonormal system on Γ . In addition, $\boldsymbol{\tau}$ is the total stress tensor, \mathbf{u} is the average displacement
 117 of the solid phase, and \mathbf{w} is the relative fluid-solid displacement.

118 As we are interested in quantifying WIFF effects on the seismoelectric signal, the re-
 119 sponse of the sample subjected to the oscillatory compressibility test is obtained by solving
 120 Biot's (1941) quasi-static equations. This approach is valid because the physical process is con-
 121 trolled by fluid-pressure diffusion and, thus, inertial effects can be neglected. In the space-frequency
 122 domain, these equations can be written as

$$123 \quad \nabla \cdot \boldsymbol{\tau} = 0, \quad (11)$$

$$124 \quad i\omega \frac{\eta}{k} \mathbf{w} = -\nabla p_f, \quad (12)$$

126 where $i = \sqrt{-1}$ is the imaginary number, ω the angular frequency, p_f the fluid pressure, k
 127 the permeability, and η the fluid viscosity. Equation (11) represents the stress equilibrium within
 128 the sample, while Eq. (12) is Darcy's law. These two equations are coupled through the stress-
 129 strain relations

$$130 \quad \boldsymbol{\tau} = (\lambda_u \nabla \cdot \mathbf{u} + \alpha_B M \nabla \cdot \mathbf{w}) \mathbf{I} + 2G^{fr} \boldsymbol{\epsilon}, \quad (13)$$

$$131 \quad p_f = -\alpha_B M \nabla \cdot \mathbf{u} - M \nabla \cdot \mathbf{w}. \quad (14)$$

133 In these equations, the involved coefficients are given by

$$134 \quad M = \left[\frac{\alpha_B - \phi}{K^s} + \frac{\phi}{K^f} \right]^{-1}, \quad (15)$$

$$135 \quad \alpha_B = 1 - \frac{K^{fr}}{K^s}, \quad (16)$$

$$136 \quad \lambda_u = K^{fr} + M \alpha_B^2 - \frac{2}{3} G^{fr}, \quad (17)$$

139 where K^{fr} , K^s , and K^f are the bulk moduli of the solid matrix, the solid grains, and the fluid
 140 phase, respectively, λ_u is the undrained Lamé constant, $\boldsymbol{\epsilon}$ is the strain tensor, ϕ is the poros-
 141 ity, and G^{fr} is the shear modulus of the bulk material, which is equal to that of the dry ma-
 142 trix.

143 The mechanical response of the sample subjected to the oscillatory compression is ob-
 144 tained by solving Eqs. (11) to (14) with the boundary conditions described by Eqs. (6) to (10).
 145 Since the methodology is based on Biot's (1941) quasi-static equations, it is limited to frequen-
 146 cies for which the resulting fluid flow is laminar. That is, the frequencies considered in the
 147 simulations should be smaller than Biot's (1962) critical frequency ω_c

$$148 \quad \omega_c = 2\pi f_c = \frac{\phi \eta}{k \rho^f}, \quad (18)$$

149 where ρ^f the density of the pore fluid.

150 In order to determine the spatial scales involved in the WIFF process in response to the
 151 applied oscillatory test, we consider a locally homogeneous medium. Without loss of gener-
 152 ality, we explore the one-dimensional case for which the solid and relative fluid displacements,

u_y and w_y , occur in the vertical direction. Combining Eqs. (11) and (13) as well as Eqs. (12) and (14) leads to

$$\nabla^2 u_y = -\frac{\alpha_B M}{H_u} \nabla^2 w_y, \quad (19)$$

and

$$i\omega \frac{\eta}{k} w_y = \alpha_B M \nabla^2 u_y + M \nabla^2 w_y, \quad (20)$$

respectively. Next, substituting Eq. (19) into Eq. (20) results in

$$i\omega w_y = D \nabla^2 w_y. \quad (21)$$

Equation (21) is a diffusion equation with the diffusivity D given by

$$D = \frac{kN}{\eta}, \quad (22)$$

where $N = M - \alpha_B^2 M^2 / H_u$, with H_u being the undrained plane-wave modulus. The spatial scale at which WIFF is significant is determined by the diffusion length

$$L_d \equiv \sqrt{D/\omega}. \quad (23)$$

2.2 Electrical response

The relative displacement between the pore fluid and the solid frame in response to the applied oscillatory compression results in a drag on the electrical excess charges of the electrical double layer (EDL). This, in turn, generates a source or streaming current density $\mathbf{J}^{i,e}$. Since the distributions of both the excess charge and the microscopic relative velocity of the pore fluid are highly dependent on their distance to the mineral grains, not all the excess charge is dragged at the same velocity. Correspondingly, a moveable charge density \hat{Q}_V^0 smaller than the total charge density \bar{Q}_V has to be considered [e.g., *Jougnot et al.*, 2012; *Revil and Mahardika*, 2013; *Revil et al.*, 2015; *Jougnot et al.*, 2015]. Note that, in the literature, the moveable charge density may also be referred to as effective excess charge and denoted by \bar{Q}_v^{eff} [e.g. *Jougnot et al.*, 2012, 2015; *Guarracino and Jougnot*]. In the considered case, the source current density takes the form [e.g., *Jardani et al.*, 2010; *Jougnot et al.*, 2013]

$$\mathbf{J}^{i,e} = \hat{Q}_V^0 i\omega \mathbf{w}, \quad (24)$$

where $i\omega \mathbf{w}$ is the relative fluid velocity. The moveable charge density formulation, which allows us to explicitly express the role played by the relative fluid velocity in the source current density generation, provides, for the same assumptions, equivalent results to the electrokinetic coupling coefficient formulation commonly used in the seismoelectric literature [e.g., *Pride*, 1994; *Jouniaux and Zyserman*, 2016]. The relationship between the moveable charge density and the electrokinetic coupling coefficient can be found in many works [e.g. *Revil and Leroy*, 2004; *Jougnot et al.*, 2012, 2015; *Revil and Mahardika*, 2013]. In the absence of an external current density, the electrical potential φ in response to a given source current density satisfies [*Sill*, 1983]

$$\nabla \cdot (\sigma^e \nabla \varphi) = \nabla \cdot \mathbf{J}^{i,e}, \quad (25)$$

where σ^e denotes the electrical conductivity, which strongly depends on the saturating pore fluid as well as on textural properties of the medium, such as the porosity and the tortuosity [e.g. *Archie*, 1942; *Clennell*, 1997; *Revil and Linde*, 2006]. As we only consider low frequencies, that is, lower than Biot's critical frequency, we assume that displacement currents can be neglected.

In conclusion, we obtain the relative fluid-solid displacement field by solving Eqs. (11) to (14) under the boundary conditions corresponding to the applied test (Eqs. 6 to 10). Next, this field is employed to determine the source current density field through Eq. (24). Finally, the electrical potential is obtained by solving Eq. (25) under pertinent boundary conditions.

2.3 Energy-based approach

The sensitivity of seismoelectric signals to parameters of interest, such as the background permeability or fracture properties, can be studied in different ways. Analytical expressions are helpful to build conceptual understanding based on idealized situations, while for more complex and realistic scenarios it is necessary to resort to numerical simulations. Typically, a particular experimental configuration is considered and differences in amplitude and spatial variations are studied [e.g., *Revil and Jardani, 2009; Jougnot et al., 2013; Grobbe and Slob, 2016*]. From a theoretical point of view, it is interesting to consider an energy-based approach and study the total energy converted into seismoelectric signals. Although it would be impossible to quantify this parameter experimentally, it constitutes an attractive theoretical approach to obtain a global estimate of the sensitivity of the method that is independent of the specific experimental configuration.

The energy density of an electric field $\mathbf{E}(t)$ is given, in the space-time domain, by [e.g. *Feynman et al., 1965*]

$$e(t) = \frac{1}{2}\varepsilon|\mathbf{E}(t)|^2, \quad (26)$$

where ε is the electric permittivity of the medium. Since displacement currents are negligible, the electric field at any time can be calculated as

$$\mathbf{E}(t) = \Re(\nabla(\varphi_0 e^{i\omega t})), \quad (27)$$

where φ_0 is the complex amplitude of the electrical potential derived for each frequency as explained in the previous section. The corresponding real part is taken because we solve the equations in the space-frequency domain.

Using average properties of time-harmonic complex-valued variables [*Rubino et al., 2006*], it is straightforward to show that

$$\langle \Re(\nabla(\varphi_0 e^{i\omega t}))^{T_p} \cdot \Re(\nabla(\varphi_0 e^{i\omega t})) \rangle = \frac{1}{2}\Re(\nabla\varphi_0^{T_p}\nabla\varphi_0^*), \quad (28)$$

where the operator $\langle \cdot \rangle$ denotes the average value over one oscillation cycle. Using Eqs. (27) and (28), we obtain

$$\langle |\mathbf{E}(t)|^2 \rangle = \frac{1}{2}|\nabla\varphi_0|^2. \quad (29)$$

Using the expression for the energy density (Eq. (26)), we finally get

$$\langle \frac{1}{2}\varepsilon|\mathbf{E}(t)|^2 \rangle = \frac{1}{4}\varepsilon|\nabla\varphi_0|^2 = \langle e(t) \rangle. \quad (30)$$

Locally, the energy density converted into seismoelectric signal in one period of oscillation T_p can therefore be computed using

$$\int_0^{T_p} e(t)dt = \frac{1}{4}\varepsilon|\nabla\varphi_0|^2 T_p. \quad (31)$$

The total converted energy in the sample can then be calculated by integrating Eq. (31) over the spatial domain. Doing so for each frequency yields a spectrum of the total converted energy. This spectroscopic analysis makes it possible to determine a frequency at which this energy is maximum over the sample. In the following, we shall refer to this as the peak frequency.

2.4 Rock physical relationships considered in this study

Our focus is on the physics governing the generation of the seismoelectric signal in response to WIFF. For this reason, we only consider clean sandstones with different porosities of the matrix and idealized rock physical relationships to link material properties. To relate

237 the porosity ϕ to the permeability k , we use the Kozeny-Carman equation [e.g., *Mavko et al.*,
238 2009]

$$239 \quad k = b \frac{\phi^3}{(1 - \phi)^2} d^2, \quad (32)$$

240 where b is a geometrical factor that depends on the tortuosity of the porous medium, and d
241 the mean grain diameter. In this analysis, we take $b = 0.003$ [*Carcione and Picotti*, 2006]
242 and $d = 8 \times 10^{-5}$ m [*Rubino et al.*, 2009]. These properties are characteristic of a well-sorted,
243 fine-grained sandstone. In addition to changes in permeability, porosity variations also imply
244 changes in the mechanical properties. To link the porosity and the solid grain properties with
245 the elastic moduli of the dry frame, we use the empirical model of *Krief et al.* [1990]

$$246 \quad K^{fr} = K^s (1 - \phi)^{3/(1-\phi)}, \quad (33)$$

$$247 \quad G^m = \frac{K^{fr} G^s}{K^s}, \quad (34)$$

248 where G^s is the shear modulus of the solid grains.

249 For the numerical study, we follow *Nakagawa and Schoenberg* [2007] and compute the
250 elastic properties of the drained fracture in terms of the shear and drained normal compliances
251

$$252 \quad \eta_T = \frac{h}{G_h^m}, \quad (35)$$

$$253 \quad \eta_N = \frac{h}{K_h^{fr} + \frac{4}{3} G_h^m}, \quad (36)$$

254 where h is the fracture aperture and K_h^{fr} and G_h^m are its drained-frame bulk and shear mod-
255 uli, respectively.

256 In this work, we consider only clean sandstones in which the surface conductivity can
257 be neglected. Also, as we consider low frequencies, that is, frequencies lower than Biot's crit-
258 ical frequency, we can safely neglect EDL polarization effects and assume that the electrical
259 conductivity has no imaginary part. Under this assumption, the electrical conductivity is given
260 by
261

$$262 \quad \sigma^e = \sigma^f \phi^{m^c} = \frac{\sigma^f}{F}, \quad (37)$$

263 where σ^f denotes the electrical conductivity of the pore water, while m^c and F are the ce-
264 mentation exponent and the formation factor as defined by *Archie* [1942], respectively. The
265 pore water conductivity depends strongly on the amount of total dissolved salts [e.g. *Sen and*
266 *Goode*, 1992].

267 The remaining electrical parameter \hat{Q}_V^0 can be obtained by employing the empirical re-
268 lationship proposed by *Jardani et al.* [2007]

$$269 \quad \log(\hat{Q}_V^0) = -9.2349 - 0.8219 \log(k), \quad (38)$$

270 where k and \hat{Q}_V^0 are in units of m^2 and C/m^3 , respectively. Below Biot's critical frequency,
271 the effective excess charge density is similar to the one at zero frequency [e.g., *Tardif et al.*,
272 2011; *Revil and Mahardika*, 2013] and, hence, boundary layer effects can be neglected in the
273 test cases considered in the following. We use idealized rock physical relationships to link σ^e
274 and \hat{Q}_V^0 to porosity, but these properties can also be inferred independently by laboratory ex-
275 periments [e.g., *Jouniaux and Pozzi*, 1995; *Suski et al.*, 2006]. Although \hat{Q}_V^0 mainly depends
276 on the permeability of the medium (Eq. 38), a recent study of *Jougnot et al.* [2015] highlighted
277 that the pore water salinity also has a significant effect on its amplitude (around one order-
278 of-magnitude change for a salinity change of four orders-of-magnitude).

The dielectric permittivity of the medium is usually expressed as the product of the dielectric permittivity of the vacuum ε_0 and the relative dielectric permittivity ε_r

$$\varepsilon = \varepsilon_r \varepsilon_0. \quad (39)$$

The parameter ε_r can be determined using a volume averaging approach [Pride, 1994; Linde *et al.*, 2006]

$$\varepsilon_r = \frac{1}{F} [\varepsilon_r^f + (F - 1) \varepsilon_r^s], \quad (40)$$

where ε_r^f and ε_r^s are the relative permittivity of the water ($\varepsilon_r^f \simeq 81$) and the solid grains ($\varepsilon_r^s \simeq 5$), respectively. This model depends on the same parameter as the electrical conductivity, that is, the formation factor (Eq. 37), and thus, is directly related to the porosity ($F = \phi^{-m^c}$).

3 Insights from 1D analytical solutions

In some simple cases, the set of equations that govern the generation of seismoelectric signals due to WIFF can be solved analytically. Equations that explicitly relate the dependence of the resulting electrical potential on rock properties can be useful to understand the underlying physical processes. Recently, *Monachesi et al.* [2015] solved the governing equations presented in the previous section for a 1D case. Here, we present their main analytical solutions and results, based on which we then study the seismoelectric signal dependence on the background permeability and on the pore water salinity.

3.1 General solution for a thin layer

Monachesi et al. [2015] consider a thin layer of thickness $2L_h$ located at the center of an otherwise homogeneous rock sample (Fig. 1). In the following, properties related to the thin layer are identified by the subscript "h" for heterogeneity and the ones corresponding to the rest of sample by the subscript "b" for background. The thicknesses of the two embedding regions constituting the background are L_b and, thus, the total thickness of the sample is $2(L_h + L_b) = L$. Assuming a set of boundary conditions analogous to Eqs. (6) to (10), the boundary value problem given by Eqs. (11) to (14) can be solved in terms of the relative fluid-solid displacement $w(y, \omega)$. Then, the current density $\mathbf{J}^{ie}(y, \omega)$ can be computed from $w(y, \omega)$ using Eq. (24). Finally, the electrical potential is obtained by solving Eq. (25) with the adequate boundary conditions. The resulting electrical potential as a function of the vertical position y and frequency ω is given by [Monachesi *et al.*, 2015]

$$\varphi(y, \omega) = \begin{cases} -\frac{i\omega\hat{Q}_V^{0,h}}{\sigma_h^e} \frac{A_h}{\kappa_h} (e^{-\kappa_h|y|} + e^{\kappa_h|y|}) + S_h, & 0 \leq |y| \leq L_h, \\ -\frac{i\omega\hat{Q}_V^{0,b}}{\sigma_b^e} \frac{A_b}{\kappa_b} (e^{-\kappa_b|y|} + e^{-\kappa_b(L-|y|)}) + S_b, & L_h \leq |y| \leq L/2, \end{cases} \quad (41)$$

where S_h , S_b , A_h , and A_b are given by

$$S_h = \frac{i\omega\hat{Q}_V^{0,h}}{\sigma_h^e} \frac{A_h}{\kappa_h} (e^{-\kappa_h L_h} + e^{\kappa_h L_h}) - \frac{i\omega\hat{Q}_V^{0,b}}{\sigma_b^e} \frac{A_b}{\kappa_b} (-\kappa_b L_h + e^{-\kappa_b(L-L_h)} - 2e^{-\kappa_b L/2}), \quad (42)$$

$$S_b = \frac{2i\omega\hat{Q}_V^{0,b}}{\sigma_b^e} \frac{A_b}{\kappa_b} e^{-\kappa_b L/2}, \quad (43)$$

$$A_h = (e^{-\kappa_h L_h} - e^{\kappa_h L_h})^{-1} \frac{\Delta P (\beta_h - \beta_b)}{\sum_{j=h,b} N_j \kappa_j \coth(\kappa_j L_j)}, \quad (44)$$

$$A_b = (e^{-\kappa_b L_h} - e^{-\kappa_b(L-L_h)})^{-1} \frac{\Delta P (\beta_h - \beta_b)}{\sum_{j=h,b} N_j \kappa_j \coth(\kappa_j L_j)}. \quad (45)$$

Note that the seismoelectric signal depends on the parameter k , which is related to the diffusion length, and, thus, among other parameters, to the permeability (see Eqs. 22 and 23) by

$$\kappa = \frac{\sqrt{i}}{L_d} = \sqrt{\frac{i\omega\eta}{kN}}, \quad (46)$$

320 and to the 1D Skempton coefficient β defined by

$$321 \quad \beta \equiv \frac{\alpha_B M}{H_u}. \quad (47)$$

322 Equation (41), together with Eqs. (42) to (45), constitute the analytical solution of the seis-
 323 moelectric response of a rock sample containing a central horizontal layer subjected to an os-
 324 cillatory compressibility test as shown in Fig. 1. It is interesting to note that the seismoelec-
 325 tric response is highly dependent on the medium permeability through $\hat{Q}_V^{0,b}$ and κ . It also de-
 326 pends on the Skempton coefficient difference between the heterogeneity and the embedding
 327 background $\beta_h - \beta_b$, and thus on the compressibility contrast between heterogeneity and back-
 328 ground. This finding is consistent with the literature on WIFF [e.g. Müller *et al.*, 2010].

329 To explore the dependence of the analytical solution on the various rock physical and
 330 structural parameters, we first consider a sample with a vertical side length of 20 cm composed
 331 of a stiff, low-permeability background with a porosity of 0.05 (Material 1 in Table 1), per-
 332 meated at its center by a compliant, high-permeability horizontal layer with a thickness of 6
 333 cm and a porosity of 0.4 (Material 2 in Table 1). The sample is fully saturated in water and
 334 subjected to a harmonic compression of amplitude $\Delta P=1$ kPa at frequencies of 10^1 , 10^2 , and
 335 10^3 Hz.

336 **Table 1.** Material properties employed in this work. Materials 1 and 2 are the same as the Materials 1 and 3
 337 used by Monachesi *et al.* [2015], respectively.

Quartz grain bulk modulus K^s [GPa]	37		
Quartz grain shear modulus G^s [GPa]	44		
Water bulk modulus K^f [GPa]	2.25		
Water viscosity η [Pa \times s]	0.001		
Water electrical conductivity σ^f [S m $^{-1}$]	0.01		
Water density ρ^f [Kg m $^{-3}$]	10^3		
	Material 1	Material 2	Material 3
Porosity ϕ	0.05	0.4	0.5
Dry rock bulk modulus K^{fr} [GPa]	31.47	2.88	0.017 / 0.04*
Dry rock shear modulus G^{fr} [GPa]	37.42	3.42	0.01 / 0.02*
Permeability k [mD]	2.66	3410	9600
Electrical conductivity σ^e [S m $^{-1}$]	2.5×10^{-5}	1.6×10^{-3}	2.5×10^{-3}
Moveable charge density \hat{Q}_V^0 [C m $^{-3}$]	526.8	1.49	0.637
Biot's critical frequency f_c [Hz]	2.99×10^6	1.8×10^4	8.29×10^3

* Calculated using Eqs. (35) and (36) for apertures of 0.03 / 0.06 cm, respectively.

338 Figure 2a shows the amplitude profile of the resulting relative fluid velocity $dw/dt =$
 339 $i\omega w$ along the y -axis ($y \in [-L/2, L/2]$) for the three frequencies considered. Due to the strong
 340 contrast between the Skempton coefficients of the two materials, significant relative fluid ve-
 341 locities arise in both the background and the layer. The relative fluid velocity is higher near
 342 the contact between the layer and the background and vanishes at the center and at both edges
 343 of the sample. Under compression, the compliant layers undergoes more deformation than the
 344 material on either side of it with the result that water is forced out of the layer. The ampli-
 345 tude of dw/dt reaches larger values for higher frequencies. A significant current density $\mathbf{J}^{1,e}$
 346 prevails in the background (Fig. 2b) due to the relative fluid velocity field (Fig. 2a) produced
 347 by the compression and the relatively large excess charge (Table 1). The maximum current
 348 densities occur at the contacts between the two materials, where the relative fluid velocity is

349 also highest. Inside the layer, even though significant fluid flow also takes place, the result-
350 ing source current density is small since the effective excess charge is much smaller in this
351 material characterized by a larger permeability (Table 1, Eq. 38).

352 Significant electrical potential amplitudes (Fig. 2c), well above the $\simeq 0.01$ mV detectabil-
353 ity threshold of laboratory experiments (e.g. *Zhu and Toksöz* [2005]; *Schakel et al.* [2012]), arise
354 in response to the oscillatory compression. These results are consistent with those by *Jou-
355 not et al.* [2013] for fractured rocks and point to the importance of WIFF effects on seismo-
356 electric signals in the presence of porosity variations. Inside the layer, the amplitude of the
357 electrical potential is constant. This is due to the negligible source current density in this high-
358 permeability material. Because the electrical potential is continuous, this corresponds to the
359 value of the electrical potential at the contact between the two materials.

360 The resulting electrical potential is not only characterized by its amplitude but also by
361 its phase θ . In the background, θ shows rapid spatial changes when the frequency is high (Fig.
362 2d). Inside the layer, θ remains constant, which is in agreement with the behavior observed
363 for the amplitude of the electrical potential in this region (Fig. 2c). In general, the phase val-
364 ues vary strongly within the medium and cover a much larger range than could be expected
365 from a frequency-dependent electrical conductivity. For example, *Kruschwitz et al.* [2010] re-
366 port a typical induced polarization phase of less than 0.6° for a large frequency range ($f \in [10^{-3};$
367 $10^4]$ Hz), while our calculations show a distribution -180 to $+180^\circ$ (Fig. 2d). This confirms
368 that our assumption concerning the negligible effect of complex conductivity at low frequen-
369 cies is valid (see section 2.4).

370 The behavior of the electrical potential curves as a function of normalized time is shown
371 in Fig. 3 for the three frequencies considered. The curves correspond to the electrical poten-
372 tial differences $\Delta\varphi$ recorded by an electrode located at the center ($y = 0$) and a reference
373 electrode located at one edge of the sample ($y = L/2$ or $y = -L/2$). Note that the integer
374 values of t/T_p correspond to the moment of maximum applied stress. This representation al-
375 lows us to interpret the physical mechanisms in a simple manner: during the compression cy-
376 cle of the applied normal stress, the fluid inside the compliant layer experiences a pressure in-
377 crease and thus water flows from the layer into the background, generating a significant seis-
378 moelectric signal. Conversely, during the extension cycle, water flows from the background
379 into the layer, generating a seismoelectric signal with an opposite sign. Note that the ampli-
380 tude and phase of the electrical potential at 10^2 and 10^3 Hz are similar with a negligible phase
381 lag with respect to the applied pressure. In contrast, the 10 Hz signal depicts different ampli-
382 tude and phase values. These differences in amplitude and phase are also evident in Figs. 2c
383 and d.

384 In order to explore in detail the dependence of the electrical potential on the frequency
385 of the oscillatory compression, we show in Fig. 4a the amplitude of the electrical potential along
386 the y -axis of the sample for frequencies between 1 Hz and 10^4 Hz [see *Monachesi et al.*, 2015,
387 for the spatial-frequency dependence of the phase]. Between ~ 10 and ~ 100 Hz, the spatial
388 extent and amplitude of the electrical potential in both the background and the layer are larger
389 than for other frequencies. It is not straightforward to assign a frequency of maximum spa-
390 tial extent since different amplitude iso-values have different corresponding frequencies of max-
391 imum spatial extent. At low frequencies (1-10 Hz), the electrical potential tends to become
392 negligible. At higher frequencies (100-10000 Hz), WIFF is comprised in the immediate vicini-
393 ty of the boundaries of the layer and the magnitude of the electrical potential is non-zero only
394 inside the layer. In agreement with Figs. 2c and d, the amplitude of the electrical potential re-
395 mains constant inside the layer at each frequency.

396 In Figure 4b we show the distribution of the electrical potential amplitude obtained when
397 the material properties of the background and the layer are interchanged. Due to the imposed
398 boundary conditions, when the layer is stiffer and less permeable than the background, the elec-
399 trical potential has a significant amplitude only inside the layer. The electrical potential am-

plitude is also frequency-dependent, with a maximum at the center of the layer and for a frequency that is higher compared to the previous situation [Monachesi *et al.*, 2015].

3.2 Particular solution for a single fracture

Monachesi *et al.* [2015] also studied the seismoelectric signal of an homogeneous rock sample that is permeated by a single horizontal fracture. This was done by adapting their analytical solution to an infinitely thin layer at the center of the sample. This yields a simpler expression of the seismoelectric response

$$\varphi(y, \omega) = -\frac{i\omega\hat{Q}_V^{0,b}}{\sigma_b^e} \frac{\bar{A}_b}{\kappa_b} \left(e^{-\kappa_b|y|} + e^{-\kappa_b(L-|y|)} - 2e^{-\kappa_b(L/2)} \right), \quad (48)$$

where

$$\bar{A}_b = \lim_{L_h \rightarrow 0} A_b = \frac{\Delta P (1 - \beta_b)}{\frac{2}{Z_N} (1 - e^{-\kappa_b L}) + N_b \kappa_b (1 + e^{-\kappa_b L})}, \quad (49)$$

and Z_N is the drained normal compliance of the fracture. Note that Z_N is the only fracture parameter in these equations, while the only structural parameter is the total thickness of the sample L . It is also interesting that the seismoelectric signal mainly depends on the background permeability k_b through κ_b (Eq. 46) and $\hat{Q}_V^{0,b}$ and on the background Skempton coefficient β_b . Figure 5a shows the spectroscopic analysis for a sample with the same size and background material as in Fig. 4a (Material 1 in Table 1) permeated by a fracture. Note the high amplitudes reached in this case due to the strong compressibility of the fracture.

3.3 Sensitivity to the background permeability

From the presented analytical solutions, it is clear that the background permeability has a predominant role in the generation of seismoelectric signals. Figure 5b shows the resulting seismoelectric signal when the background permeability is one order-of-magnitude larger than in Material 1, that is, $k_b = 26.6$ mD. As opposed to what was presented by Monachesi *et al.* [2015], we let the permeability vary independently of the porosity, which does not change, so that the changes observed are uniquely related to permeability changes. We can observe two different effects: as the permeability increases, the maximum amplitude of the signal increases and the frequency of maximum extent of the signal is shifted towards higher frequencies. This result is consistent with the ones discussed by Jougnot *et al.* [2013]. The spatial scale at which WIFF occurs depends on the diffusion length and, therefore, on the background permeability (Eq. 46). Therefore, the frequency of maximum extent of the signal is mainly controlled by the background hydraulic properties, which is consistent with the asymptotic analysis by Monachesi *et al.* [2015]. The shift of maximum WIFF to higher frequencies related to a larger permeability also implies a higher fluid velocity and thus a higher amplitude of the electrical potential (Fig. 2). The amplitude of the seismoelectric signal is also affected by the imposed relationship between the moveable charge density and the background permeability (Eq. 38). A larger permeability implies a smaller moveable charge density and thus a decrease of the amplitude. The significant increase in amplitude shown in Fig. 5b suggests that the effect of a larger fluid velocity due to the shift to higher frequencies dominates over the amplitude decrease due to the smaller moveable charge density.

3.4 Sensitivity to the pore water conductivity

The moveable charge density is not only influenced by the permeability. As discussed by Jougnot *et al.* [2015], the pore water salinity, and thus the pore water electrical conductivity σ^f , also affects their moveable charge density through its influence on the thickness of the EDL and the associated changes of the Zeta potential [e.g. Revil *et al.*, 1999]. In addition, the pore water conductivity also strongly affects the bulk electrical conductivity (Eq. 37). To study the effect of salinity changes on the seismoelectric signal, we complement our spectroscopy analysis for a pore water conductivity that is one order-of-magnitude smaller ($\sigma^f = 0.001$ S

446 m^{-1} , Fig. 6a) and one order-of-magnitude larger ($\sigma^f = 0.1 \text{ S m}^{-1}$, Fig. 6b) than in the pre-
447 vious cases ($\sigma^f = 0.01 \text{ S m}^{-1}$, Fig. 5a). We calculate the corresponding moveable charge density
448 as deviations from the value given by Eq. (38) with the model proposed by *Jougnot et al.*
449 [2015]. This results in values of $\hat{Q}_V^{0,b} = 790.12 \text{ C m}^{-3}$ and 351.31 C m^{-3} , for $\sigma^f = 0.001 \text{ S}$
450 m^{-1} , and $\sigma^f = 0.1 \text{ S m}^{-1}$, respectively. Not surprisingly, the impact of salinity/pore water con-
451 ductivity upon the seismoelectric signal is significant: the lower the pore water conductivity,
452 the higher the amplitude of the signal. The frequency of maximum extent of the signal is not
453 affected by a change in pore water conductivity. Note here that the influence of fluid conduc-
454 tivity on the seismoelectric response is more important due to its effect on the bulk electri-
455 cal conductivity (Eq. 37) than to its impact on $\hat{Q}_V^{0,b}$, which can be considered a secondary ef-
456 fect [*Jougnot et al.*, 2015].

457 4 Numerical study of fractured rock samples

458 In this section, we numerically solve the governing equations described in the theory sec-
459 tion in order to consider 2D fracture geometries. We employ the numerical strategy presented
460 by *Jougnot et al.* [2013] for exploring the generation of seismoelectric signals due to WIFF
461 in the presence of fractures. That is, we consider a 2D synthetic rock sample containing meso-
462 scopic heterogeneities. Equations (11) to (14) are solved, with the boundary conditions described
463 by Eqs. (6) to (10), using a finite element procedure [*Rubino et al.*, 2009]. From the result-
464 ing 2D velocity fields, we compute the electrical current density (Eq. 24) and then numeri-
465 cally solve Eq. (25) assuming perfect electrical insulation along the boundaries using a finite
466 volume approach. To do so, we adapted an open source finite volume numerical code that was
467 originally conceived to solve subsurface fluid flow problems [*Künze et al.*, 2014] to the con-
468 sidered electrical problem. In an initial analysis, we consider a synthetic homogeneous rock
469 sample containing a simple 2D fracture. We then study the effects of different fracture lengths,
470 different fracture orientations, and different numbers of fractures in the sample. Finally, frac-
471 ture networks with varying degrees of connectivity are explored.

472 4.1 Analysis for a single fracture

473 We first consider a simple case corresponding to a homogeneous rock containing a hori-
474 zontal fracture at its center (Fig. 7a). For the background material, we use for all cases the
475 same sandstone as in the analytical study (Material 1 in Table 1). The fracture is modeled as
476 a very compliant poroelastic rectangle that is characterized by large values of porosity and per-
477 meability (Material 3 in Table 1), with the elastic properties being calculated using Eqs. (35)
478 and (36). Given that the fracture does not permeate the entire sample, the analytical solution
479 presented in the previous section cannot be used and, instead, the numerical approach is em-
480 ployed. This initial case will be the basic geometry for which we will perform the 2D sen-
481 sitivity analysis.

482 We consider a sample of $6 \times 6 \text{ cm}^2$ with a horizontal fracture of 3 cm length and 0.03
483 cm aperture located at its center (Fig. 7a). We use 600×600 elements to discretize the en-
484 tire domain. The numerical simulations using this mesh were compared to simulations using
485 finer meshes to ensure the accuracy of the calculations. We compute the seismoelectric response
486 of oscillatory compressions with $\Delta P = 1 \text{ kPa}$ at 40 different frequencies equally spaced on
487 a logarithmic scale between 1 and 10000 Hz.

488 Figure 7b shows the resulting seismoelectric signal amplitude for a frequency of 142 Hz.
489 Note that the electrical problem has been solved using a reference electrode at the origin (x
490 $= 0 \text{ cm}$, $y = 0 \text{ cm}$). The electrical potential generated by this small heterogeneity is maximal
491 in the immediate vicinity of the fracture and easily measurable with typical experimental set-
492 up in the laboratory. This large signal is due to the high compressibility contrast between the
493 fracture and the background, which in turn results in significant WIFF.

494 In Fig. 7, we display the detailed spatial distribution of the electrical potential for a sin-
495 gular frequency in order to stress the 2D nature of the signal. However, the main interest of our
496 approach is to study the spectral dependence of the signal generated by the oscillatory com-
497 pression through a spectroscopic analysis. In order to best represent these results, Figure 8a
498 shows vertical cuts of the seismoelectric signal amplitude through the center of the sample shown
499 in Fig. 7a ($x = 3$ cm) as a function of frequency. These vertical cuts, which pass through the
500 center of the fracture, are similar to those presented in the analytical section, but it should be
501 noted that in this case the sample is 2D. To complete our study, we use the results of the energy-
502 based analysis that we developed in Section 2.3 to provide a global measure of the frequency
503 dependence of the seismoelectric signal in the sample. Figure 8b shows the total energy con-
504 verted to the seismoelectric signal in one compression cycle as a function of frequency. To cal-
505 culate this value, we numerically computed for each frequency the gradient of the electrical
506 potential amplitude (Eq. 31) and summed the squared contribution of each pixel weighted by
507 its electrical permittivity (Eqs. (39) and (40)) multiplied by one fourth of the corresponding
508 period. The resulting spectrum shows a strong dependence of the converted electric energy on
509 frequency and a clearly defined peak frequency for which the converted electric energy is max-
510 imum. In this case, the peak frequency corresponds to 142 Hz, which is the frequency used
511 for the 2D representation in Fig. 7b.

512 4.2 Sensitivity to the fracture length

513 In this subsection, we investigate the effect of the fracture extent along the x -axis in the
514 sample on the amplitude of the seismoelectric signal. We consider two cases where the frac-
515 ture length is smaller than in the previous section, with fracture lengths of 0.6 and 1.8 cm (Figs.
516 9a and d, respectively), and two cases where the extent is larger, that is, 4.2 and 6 cm (Figs.
517 9g and j, respectively). The latter corresponds to the extreme case of a fracture that perme-
518 ates the whole sample. As the fracture length increases, so does the spectral range at which
519 the fracture can be detected, the amplitude of the signal, and the vertical extent of the mea-
520 surable electrical potential (Figs. 9b, e, h, and k). From the converted energy (Figs. 9c, f, i,
521 and l) we can also see that the fracture length changes the peak frequency at which the con-
522 verted energy is higher; larger fractures imply a lower peak frequency and a higher amount
523 of converted energy. Note that a one order-of-magnitude change in the fracture length from
524 the sample in Fig. 9a to the one in Fig. 9j implies a shift of almost two orders-of-magnitude
525 in the peak frequency and an increase of more than two orders-of-magnitude in the converted
526 energy.

527 4.3 Sensitivity to the fracture orientation

528 To understand the sensitivity to the fracture orientation, we consider four cases where
529 a 3 cm long fracture is oriented from sub-horizontal to vertical with respect to the x -axis (see
530 Figs. 10a, d, g, j and the figure caption for the fracture angles). As the orientation of the frac-
531 ture becomes more vertical, the amplitude of the electrical potential decreases. WIFF takes
532 place from the more compliant fracture to the stiff background and vice versa, and is max-
533 imum when the fracture is perpendicular to the direction of applied stress. In the horizontal
534 case, the applied stress strongly deforms the fracture, increases its fluid pressure and produce
535 significant WIFF and seismoelectric conversion. Conversely, in the extreme case of a verti-
536 cal fracture, the fluid mainly flows inside the fracture, which has a low $\hat{Q}_V^{0,h}$ and therefore it
537 does not produce a significant electrical source current density. The intermediate states (Figs.
538 10a, d, and g) show the smooth transition between a horizontal to a vertical fracture. The ori-
539 entation does not affect the peak frequency, although the total converted energy is, as expected,
540 significantly smaller for more vertically oriented fractures (Figs. 10 c, f, i and l).

4.4 Sensitivity to the number of fractures

To understand the aggregate effect of multiple fractures, we consider an increasing amount of fractures in a sample of the same size as in the previous cases. The starting point is a single fracture as shown in the fracture length subsection (Fig. 9j). We then consider cases with 2, 3, 4 and 5 equally spaced fractures throughout the sample (Figs. 11 a, d, g, and j). The corresponding fracture spacings are 2.97, 1.97, 1.47, and 1.17 cm, respectively. Regardless of the number of fractures in the sample, the maximum amplitude of electrical potential does not significantly change. As the number of fractures in the sample increases, the vertical extent of the seismoelectric signal generated by each fracture decreases and the spectral range where the signal could be detected is shifted towards higher frequencies. Correspondingly, the energy plots in Fig. 11 show that the peak frequency for which the maximum of energy is converted also shifts to higher values as the number of fracture increases. This shift in frequency corresponds to the dependence of the diffusion length (Eq. 23) on the frequency; by decreasing the space between fractures, we decrease the spatial scale at which WIFF between the fractures can take place, thus the frequency corresponding to the maximum extent of fluid flow is higher. It is interesting to note that although the peak frequency is affected by the number of fractures in the sample, this parameter does not seem to influence the total converted energy at the corresponding peak frequency (Fig. 11). This suggests that the larger number of fractures compensates for the smaller spatial extent of the region in which significant electrical potential amplitude are produced by each fracture in the sample.

4.5 Analysis of a fracture network

In this subsection, we study the effects of fracture connectivity on the seismoelectric signal. We consider a similar setup as the one used by *Rubino et al.* [2014] to explore the dependence of the seismic attenuation on fracture connectivity. We consider a sample of 20×20 cm², discretized by 1000×1000 elements, and examine four different fracture scenarios. In the first scenario, horizontal fractures are randomly distributed in the sample (Fig. 12a). In the second scenario, the horizontal fractures are retained and vertical fractures are added randomly under the constraint that none of the fractures is connected to another one (Fig. 12c). The third case corresponds to the same number of horizontal and vertical fractures, but with some of the vertical fractures being connected to the horizontal ones (Fig. 12e). Finally, in the fourth scenario we consider the case when all the vertical fractures are connected to some of the horizontal ones (Fig. 12g). In all the examples, the fractures have an aperture of 0.06 cm. The fracture properties are given in Table 1 (Material 3). The maximum pressure applied is the same as in all other examples, that is, $\Delta P = 1$ kPa, and all the boundary conditions remain the same as in previous cases.

Figure 12 shows the amplitude of the electrical potential of the four geometries considered for a frequency of 0.73 Hz. We observe that the presence of vertical fractures that are not connected to the horizontal ones does not significantly change the amplitude of the seismoelectric response (Figs. 12b and d). However, when the vertical fractures are connected to the horizontal ones, the spatial distribution and amplitude of the electrical potential does change (Figs. 12f and h). Indeed, the maximum amplitude in the sample is lower for a higher fracture connectivity and larger parts of the sample are “illuminated” with a measurable electrical potential in this case.

To study the dependence of the seismoelectric signal on fracture connectivity at the sample scale, we present in Fig. 13 plots of the total converted electrical energy as a function of frequency. A clear dependence on fracture connectivity can be observed. Adding the unconnected vertical fractures results in a higher seismoelectric energy, but as the fracture connectivity increases, there is a decrease in the total energy of the electric field. The peak frequency is also affected by the degree of connectivity. When the vertical unconnected fractures are added, the peak frequency does not change and corresponds to 0.73 Hz, which was the frequency used in Fig. 12. Increasing the fracture connectivity shifts the peak frequency to higher values.

5 Discussion and conclusions

Following *Jougnot et al.* [2013] and *Monachesi et al.* [2015], we performed a theoretical (analytical and numerical) study of the seismoelectric signals generated when a rock sample containing mesoscopic heterogeneities is submitted to an oscillatory compressibility test. Heterogeneities are considered mesoscopic when their size is smaller than the typical wavelength but larger than the pore-scale. In the present contribution we focused on mesoscopic-scale fractured media and developed a quantitative approach to characterize the dependence of the seismoelectric signal with fracture connectivity. The predicted signal is highly frequency-dependent and hence we illustrated our results in terms of the space-frequency distribution of the seismoelectric response, which corresponds to a spectroscopic analysis. The source of this frequency-dependent signal is linked to WIFF from the more compliant heterogeneities to the background during the compression cycle, and in the opposite direction during the dilatation cycle. Our results show that this phenomenon yields measurable seismoelectric signals under typical laboratory set-ups in terms of applied pressure, frequency range, and instrument resolution [e.g. *Batzle et al.*, 2006; *Subramanian et al.*, 2014; *Pimienta et al.*, 2015].

We introduced for the first time an energy-based approach (Section 2.3) to characterize the seismoelectric conversion at the sample scale. This approach provides complementary information to our spectroscopic analysis at the sample scale by allowing for the definition of a peak frequency for which the total converted seismoelectric energy is maximum. The total converted seismoelectric energy could be compared to the elastic strain energy and energy dissipation as derived by *Solazzi et al.* [2016]. This is, however, outside the scope of this contribution and we leave this comparison for future publications.

We studied different kinds of mesoscopic heterogeneities: thin layers, single fractures and fracture networks. Our results show a strong dependence of the seismoelectric signal on mechanical, hydraulic, and structural properties of the background and the mesoscopic heterogeneities. In particular, the background permeability via the diffusion length, fracture separation and fracture length, control the frequency at which maximum WIFF occurs and, therefore, also influences the peak frequency. The amplitude of the electrical potential is mainly controlled by the background permeability, the pore water conductivity, compressibility contrast between heterogeneity and background, and fracture orientation. These parameters affect the bulk conductivity, movable charge density, and source current density, which define the electrical potential distribution in the sample. Similar to what was observed by *Rubino et al.* [2013, 2014] for the seismic case, fracture orientation, extent, density, and connectivity influence the spectroscopic signature of the seismoelectric signal. This is particularly interesting for the characterization of fractured media, which is of primary importance in hydrological applications yet extremely difficult to achieve in practice [e.g. *Berkowitz*, 2002].

Connected fractures reduce the total energy converted to the seismoelectric signal and change the spatial distribution of electrical potential amplitude. For an equal number of horizontal and vertical fractures, the total converted electrical energy decreases by $\sim 50\%$ for the corresponding peak frequency (Fig. 13) when these fractures are connected. The reason for this is that the connection to vertical fractures enables part of the fluid pressure increase in response to the applied stress to be released from the horizontal fractures into these highly permeable regions. This reduces the fluid pressure gradient and, thus, the fluid flow between fractures and background, which in turn results in a decrease of the generated electrical source current density and the measurable electrical potential outside the fractures. Given that the degree of fracture connectivity controls the effective hydraulic properties of fractured rocks, this connectivity effects are potentially important as they may help to extract this kind of information from corresponding seismoelectric measurements.

The present contribution describes analytical and numerical experiments and aims at understanding how mesoscopic heterogeneities can produce measurable seismoelectric signals under laboratory conditions. To the best of the author's knowledge, these prediction have not yet been tested in practice. Such experimental studies would be of significant interest for both

644 the rock physics and the seismoelectric community as they may provide a new rock physical
645 characterization tool: seismoelectric spectroscopy.

646 Besides thin layers or fractures, other types of mesoscopic heterogeneities are known to
647 generate significant WIFF [e.g. *Batzle et al.*, 2006; *Adam et al.*, 2009; *Müller et al.*, 2010; *Pimienta*
648 *et al.*, 2015] but remain unexplored in terms of their seismoelectric response. Similar effects
649 also exist in patch-type partially saturated conditions [e.g. *Caspari et al.*, 2011; *Masson and*
650 *Pride*, 2011; *Rubino and Holliger*, 2012]. Such saturation effects and the resulting seismoelec-
651 tric signals could explain some discrepancies between experimental data and current models,
652 such as those shown by *Bordes et al.* [2015].

653 The results of this study could also help to better understand seismoelectric conversions
654 at the field scale. Indeed, all geological formations contain a certain degree of mesoscopic het-
655 erogeneity and, therefore, seismic waves are expected to produce seismoelectric signals asso-
656 ciated with such heterogeneities as they propagate. These phenomena could be one of the causes
657 for the difficulties encountered in seismoelectric field applications. For example, high noise
658 levels encountered in field applications [e.g. *Strahser et al.*, 2011] could be related to hetero-
659 geneities of different nature and size that generate multiple seismoelectric source currents when
660 traversed by the seismic waves. Further studies accounting for effects such as geometrical di-
661 vergence and the co-seismic field will be carried out in the near future. These are necessary
662 to quantify the relative contribution of Biot's slow waves to the total seismoelectric signal that
663 would be measured in the field. Our results clearly illustrate that a better understanding of the
664 role played by mesoscopic heterogeneities is essential for the development of the seismoelec-
665 tric method.

666 **Acknowledgments**

667 This work was partly financed by the Swiss National Science Foundation. This is IGP contribution number 3893.
668

669 **References**

- 670 Adam, L., M. Batzle, K. Lewallen, and K. van Wijk (2009), Seismic wave attenuation in
671 carbonates, *J. Geophys. Res.*, *114*(B6), 6208.
- 672 Archie, G. (1942), The electrical resistivity log as an aid in determining some reservoir
673 characteristics, *Trans. Ame. Inst. of Min. and Metall. Eng.*, *146*, 54–61.
- 674 Batzle, M., D. Han, and R. Hofmann (2006), Fluid mobility and frequency-dependent
675 seismic velocity - Direct measurements, *Geophysics*, *71*(1), N1–N9.
- 676 Berkowitz, B. (2002), Characterizing flow and transport in fractured geological media: A
677 review, *Adv. Water Resour.*, *25*(8), 861–884.
- 678 Biot, M. (1941), General theory of three-dimensional consolidation, *J. Appl. Phys.*, *12*,
679 155–164.
- 680 Biot, M. (1962), Mechanics of deformation and acoustic propagation in porous media, *J.*
681 *Appl. Phys.*, *33*, 1482–1498.
- 682 Bordes, C., P. Sénéchal, J. Barrière, D. Brito, E. Normandin, and D. Jougnot (2015),
683 Impact of water saturation on seismoelectric transfer functions: A laboratory study of
684 coseismic phenomenon, *Geophys. J. Int.*, *200*(3), 1317–1335.
- 685 Carcione, J., and S. Picotti (2006), P-wave seismic attenuation by slow-wave diffusion:
686 Effects of inhomogeneous rock properties, *Geophysics*, *71*, O1–O8.
- 687 Caspari, E., T. Müller, and B. Gurevich (2011), Time-lapse sonic logs reveal patchy CO₂
688 saturation in-situ, *Geophys. Res. Lett.*, *38*, L13,301.
- 689 Clennell, M. B. (1997), Tortuosity: a guide through the maze, *Geol. Soc., London, Spec.*
690 *Publ.*, *122*(1), 299–344.
- 691 Feynman, R., A. R. Hibbs, R. Leighton, M. Sands, and E. Hafner (1965), The Feynman lectures
692 on physics, Part I, Prentice-Hall, Englewood Cliffs, N.J., 520 pp.

- 693 Grobbe, N., and E. Slob (2016), Seismo-electromagnetic thin-bed responses: Natural
694 signal enhancements?, *J. Geophys. Res.*, *121*(4), 2460–2479.
- 695 Guarracino, L., and D. Jougnot (), A physically based analytical model to describe effec-
696 tive excess charge for streaming potential generation in water saturated porous media,
697 *Journal of Geophysical Research: Solid Earth*, pp. n/a–n/a, doi:10.1002/2017JB014873,
698 2017JB014873.
- 699 Haartsen, M., and S. Pride (1997), Electro seismic waves from point sources in layered
700 media, *J. Geophys. Res.*, *102*(B11), 24,745–24,769.
- 701 Haines, S. S., and S. R. Pride (2006), Seismoelectric numerical modeling on a grid, *Geo-*
702 *physics*, *71*(6), N57–N65.
- 703 Jardani, A., A. Revil, A. Bolève, A. Crespy, J. Dupont, W. Barrash, and B. Malama
704 (2007), Tomography of the darcy velocity from self-potential measurements, *Geophys.*
705 *Res. Lett.*, *34*(24), L24,403.
- 706 Jardani, A., A. Revil, E. Slob, and W. Söllner (2010), Stochastic joint inversion of 2D
707 seismic and seismoelectric signals in linear poroelastic materials: A numerical investiga-
708 tion, *Geophysics*, *75*(1), N19–N31.
- 709 Jougnot, D., N. Linde, A. Revil, and C. Doussan (2012), Derivation of soil-specific
710 streaming potential electrical parameters from hydrodynamic characteristics of partially
711 saturated soils, *Vadose Zone J.*, *11*(1), doi:10.2136/vzj2011.0086.
- 712 Jougnot, D., J. G. Rubino, M. Rosas-Carbajal, N. Linde, and K. Holliger (2013), Seismo-
713 electric effects due to mesoscopic heterogeneities, *Geophys. Res. Lett.*, *40*(10), 2033–
714 2037.
- 715 Jougnot, D., N. Linde, E. Haarder, and M. Looms (2015), Monitoring of saline tracer
716 movement with vertically distributed self-potential measurements at the HOBE agricul-
717 tural test site, vouldund, denmark, *J. Hydro.*, *521*(0), 314 – 327.
- 718 Jouniaux, L., and J. Pozzi (1995), Streaming potential and permeability of saturated
719 sandstones under triaxial stress: Consequences for electrotelluric anomalies prior to
720 earthquakes, *Journal of geophysical research*, *100*(B6), 10,197–10.
- 721 Jouniaux, L., and F. Zyserman (2016), A review on electrokinetically induced seismo-
722 electrics, electro-seismics, and seismo-magnetics for earth sciences, *J. Geophys. Res.*,
723 *7*(1), 249–284.
- 724 Krief, M., J. Garat, J. Stellingwerff, and J. Ventre (1990), A petrophysical interpretation
725 using the velocities of P and S waves (full waveform inversion), *The Log Analyst*, *31*,
726 355–369.
- 727 Kruschwitz, S., A. Binley, D. Lesmes, and A. Elshenawy (2010), Textural controls on
728 low-frequency electrical spectra of porous media, *Geophysics*, *75*(4), WA113–WA123.
- 729 Künze, R., P. Tomin, and I. Lunati (2014), Local modeling of instability onset for global
730 finger evolution, *Adv. Water Resour.*, *70*, 148–159.
- 731 Linde, N., A. Binley, A. Tryggvason, L. Pedersen, and A. Revil (2006), Improved hydro-
732 geophysical characterization using joint inversion of cross-hole electrical resistance and
733 ground-penetrating radar travelttime data., *Water Resour. Res.*, *42*(12), W04,410.
- 734 Masson, Y., and S. Pride (2011), Seismic attenuation due to patchy saturation, *J. Geophys.*
735 *Res.*, *116*, B03,206.
- 736 Masson, Y. J., and S. R. Pride (2007), Poroelastic finite difference modeling of seismic at-
737 tenuation and dispersion due to mesoscopic-scale heterogeneity, *Journal of Geophysical*
738 *Research: Solid Earth*, *112*(B3).
- 739 Mavko, G., T. Mukerji, and J. Dvorkin (2009), *The Rock Physics Handbook: Tools for*
740 *Seismic Analysis of Porous Media*, Cambridge University Press.
- 741 Monachesi, L. B., J. G. Rubino, M. Rosas-Carbajal, D. Jougnot, N. Linde, B. Quintal,
742 and K. Holliger (2015), An analytical study of seismoelectric signals produced by 1-D
743 mesoscopic heterogeneities, *Geophys. J. Int.*, *201*(1), 329–342.
- 744 Müller, T., and B. Gurevich (2005), Wave-induced fluid flow in random porous media:
745 Attenuation and dispersion of elastic waves, *J. Acoust. Soc. Amer.*, *117*, 2732–2741.

746 Müller, T., B. Gurevich, and M. Lebedev (2010), Seismic wave attenuation and disper-
747 sion resulting from wave-induced flow in porous rocks - A review, *Geophysics*, 75,
748 A147–A164.

749 Nakagawa, S., and M. Schoenberg (2007), Poroelastic modeling of seismic boundary
750 conditions across a fracture, *J. Acoust. Soc. America*, 122, 831–847.

751 Pimienta, L., J. Fortin, and Y. Guéguen (2015), Bulk modulus dispersion and attenuation
752 in sandstones, *GEOPHYSICS*, 80(2), D111–D127, doi:10.1190/geo2014-0335.1.

753 Pride, S. (1994), Governing equations for the coupled electromagnetics and acoustics of
754 porous media, *Phys. Rev.*, 50(21), 15,678–15,696.

755 Revil, A., and A. Jardani (2009), Seismoelectric response of heavy oil reservoirs: theory
756 and numerical modelling, *Geophys. J. Int.*, 180(2), 781–797.

757 Revil, A., and P. Leroy (2004), Constitutive equations for ionic transport in porous shales,
758 *J. Geophys. Res.*, 109(B3), B03,208.

759 Revil, A., and N. Linde (2006), Chemico-electromechanical coupling in microporous
760 media, *J. Coll. Interf. Sci.*, 302(2), 682–694.

761 Revil, A., and H. Mahardika (2013), Coupled hydromechanical and electromagnetic
762 disturbances in unsaturated porous materials, *Water Resour. Res.*, pp. 744–766, doi:
763 10.1002/wrcr.20092.

764 Revil, A., P. Pezard, and P. Glover (1999), Streaming potential in porous media: 1. theory
765 of the zeta potential, *J. Geophys. Res.*, 104(B9), 20,021–20,031.

766 Revil, A., A. Jardani, P. Sava, and A. Haas (2015), *The Seismoelectric Method: Theory and*
767 *Application*, John Wiley & Sons.

768 Rubino, J., and K. Holliger (2012), Seismic attenuation and velocity dispersion in hetero-
769 geneous partially saturated porous rocks, *Geophys. J. Int.*, 188, 1088–1102.

770 Rubino, J., C. Ravazzoli, and J. Santos (2009), Equivalent viscoelastic solids for heteroge-
771 neous fluid-saturated porous rocks, *Geophysics*, 74, N1–N13.

772 Rubino, J., T. M. Müller, L. Guarracino, M. Milani, and K. Holliger (2014), Seismoacous-
773 tic signatures of fracture connectivity, *J. Geophys. Res.*, 119(3), 2252–2271.

774 Rubino, J. G., C. L. Ravazzoli, and J. E. Santos (2006), Reflection and transmission of
775 waves in composite porous media: A quantification of energy conversions involving
776 slow waves, *J. Acoust. Soc. Am.*, 120(5), 2425–2436.

777 Rubino, J. G., L. Guarracino, T. M. Müller, and K. Holliger (2013), Do seismic waves
778 sense fracture connectivity?, *Geophys. Res. Lett.*, doi:10.1002/grl.50127.

779 Schakel, M., D. Smeulders, E. Slob, and H. Heller (2012), Seismoelectric fluid/porous-
780 medium interface response model and measurements, *Transp. Por. Med.*, 93(2), 271–
781 282.

782 Sen, P. N., and P. A. Goode (1992), Influence of temperature on electrical conductivity on
783 shaly sands, *Geophysics*, 57(1), 89–96.

784 Sill, W. (1983), Self-potential modeling from primary flows, *Geophysics*, 48(1), 76–86,
785 doi:10.1190/1.1441409.

786 Solazzi, S. G., J. G. Rubino, T. M. Müller, M. Milani, L. Guarracino, and K. Holliger
787 (2016), An energy-based approach to estimate seismic attenuation due to wave-induced
788 fluid flow in heterogeneous poroelastic media, *Geophys. J. Int.*, 207(2), 823–832.

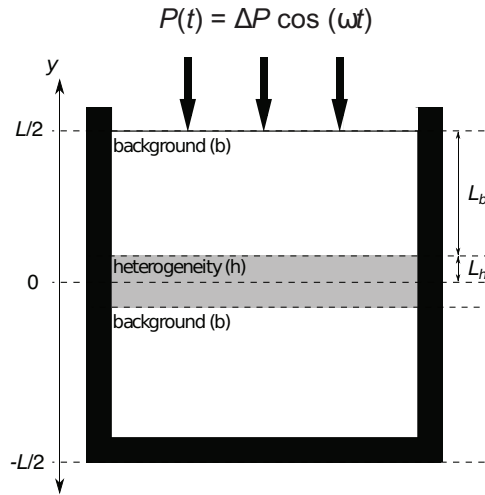
789 Strahser, M., L. Jouniaux, P. Sailhac, P. Matthey, and M. Zillmer (2011), Dependence of
790 seismoelectric amplitudes on water content, *Geophys. J. Int.*, 187(3), 1378–1392.

791 Subramaniyan, S., B. Quintal, N. Tisato, E. H. Saenger, and C. Madonna (2014), An
792 overview of laboratory apparatuses to measure seismic attenuation in reservoir rocks,
793 *Geophys. Prospect.*, 62(6), 1211–1223.

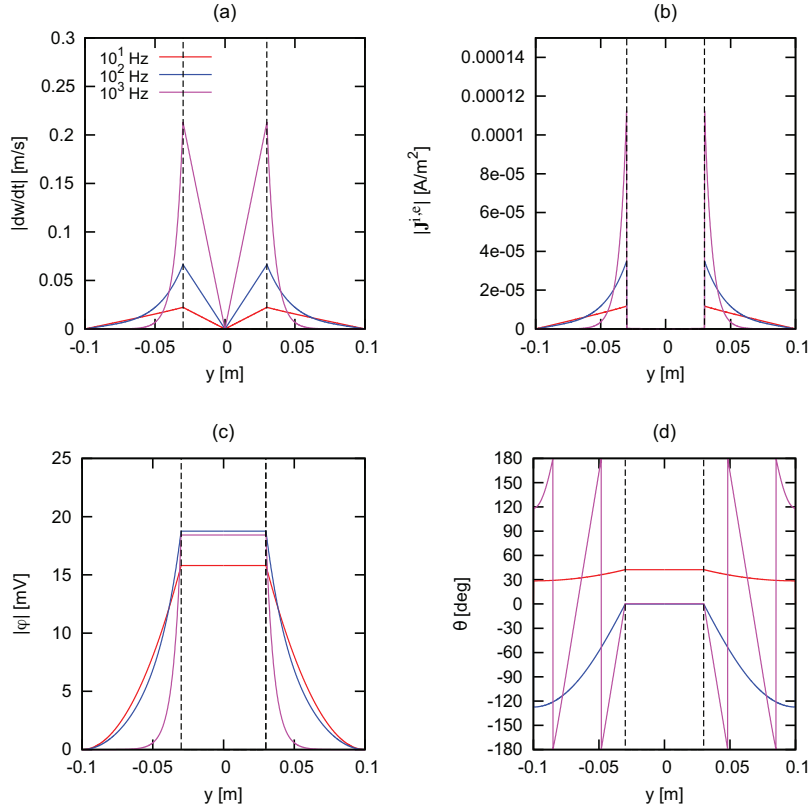
794 Suski, B., A. Revil, K. Titov, P. Konosavsky, M. Voltz, C. Dages, and O. Huttel (2006),
795 Monitoring of an infiltration experiment using the self-potential method, *Water Resour.*
796 *Res.*, 42(8), W08,418.

797 Tardif, E., P. W. Glover, and J. Ruel (2011), Frequency-dependent streaming potential of
798 ottawa sand, *J. Geophys. Res.*, 116(B4).

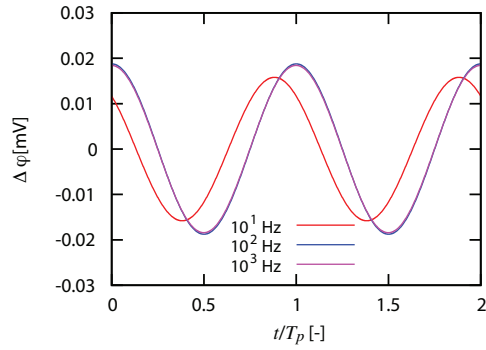
799 Tisato, N., and C. Madonna (2012), Attenuation at low seismic frequencies in partially
 800 saturated rocks: Measurements and description of a new apparatus, *J. Appl. Geophys.*,
 801 86, 44–53.
 802 Zhu, Z., and M. Toksöz (2005), Seismoelectric and seismomagnetic measurements in
 803 fractured borehole models, *Geophysics*, 70(4), F45–F51, doi:10.1190/1.1996907.
 804 Zyserman, F. I., P. M. Gauzellino, and J. E. Santos (2010), Finite element modeling of
 805 SHTE and PSVTM electroseismics, *J. Appl. Geophys.*, 72(2), 79–91.



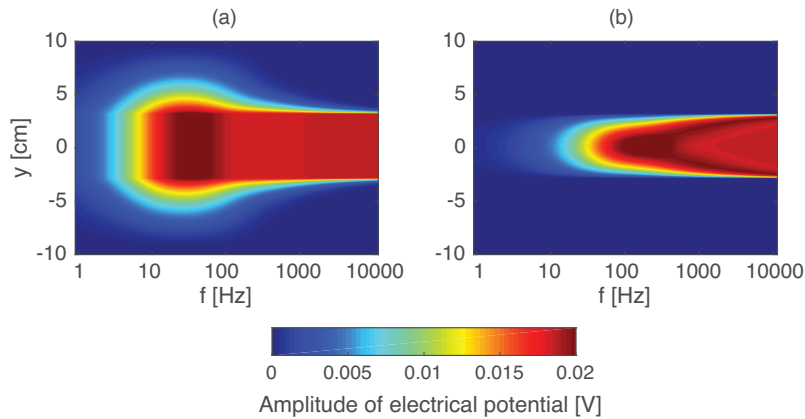
806 **Figure 1.** Schematic representation of the oscillatory compressibility test proposed by *Jougnot et al.* [2013]
 807 applied to a sample containing a single layer.



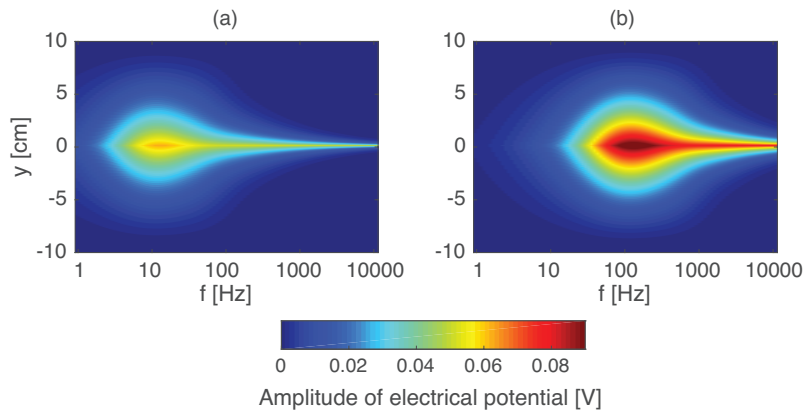
808 **Figure 2.** (a) Amplitude of relative fluid velocity dw/dt , (b) amplitude of electrical source current density
809 $\mathbf{J}^{i,e}$, and (c) amplitude $|\varphi|$ and (d) phase θ of the electrical potential corresponding to a rectangular, stiff, low-
810 permeability background containing a compliant, high-permeability horizontal layer at its center. The porosity
811 of the layer is 0.4 (Material 2 in Table 1), whereas that of the background is 0.05 (Material 1 in Table 1). In all
812 cases, the panels show the parameters as functions of y . For visualization purposes, we denote the boundaries
813 of the layer by dashed lines.



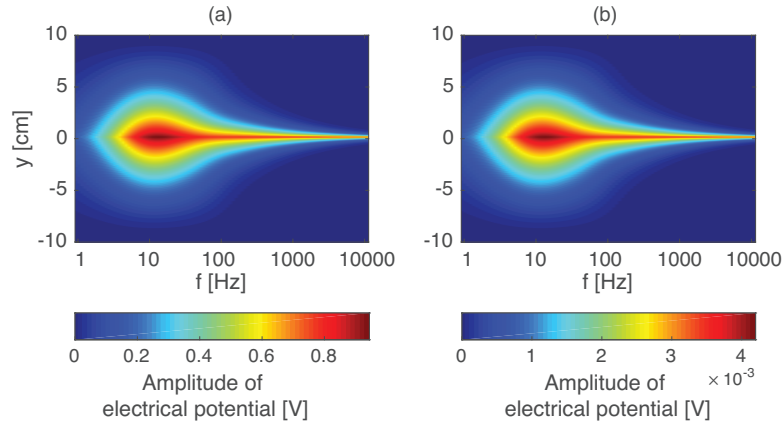
814 **Figure 3.** Electrical potential differences $\Delta\varphi$ between an electrode located at the center of the sample and a
 815 reference electrode located at an edge of the sample as functions of the normalized time t/T_p for frequencies
 816 of 10^1 , 10^2 , and 10^3 Hz.



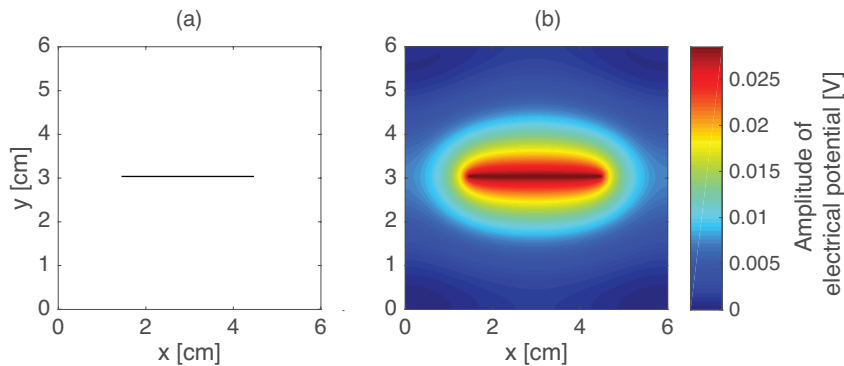
817 **Figure 4.** Amplitude of the electrical potential along the y -axis as a function of frequency corresponding
 818 to (a) a stiff, low-permeability background containing a compliant, high-permeability horizontal layer at its
 819 center, and (b) a compliant, high-permeability background containing a stiff, low-permeability horizontal
 820 layer at its center. Adapted from *Monachesi et al.* [2015].



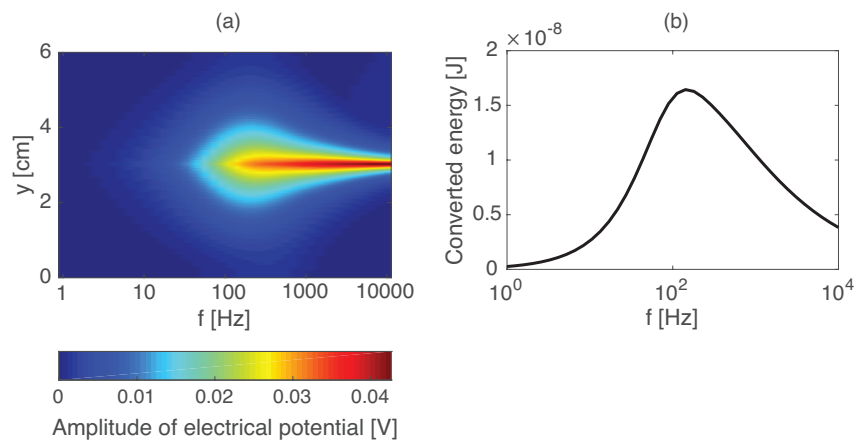
821 **Figure 5.** Seismoelectric response of a sample containing a fracture at its center (Eqs. 48 and 49) and
 822 its dependence on the background permeability. Amplitude of the electrical potential along the y -axis as a
 823 function of frequency (a) for the background properties corresponding to Material 1 (Table 1, $k_b = 2.66$ mD)
 824 and (b) for a background permeability that is one order-of-magnitude larger ($k_b = 26.6$ mD). Adapted from
 825 *Monachesi et al.* [2015].



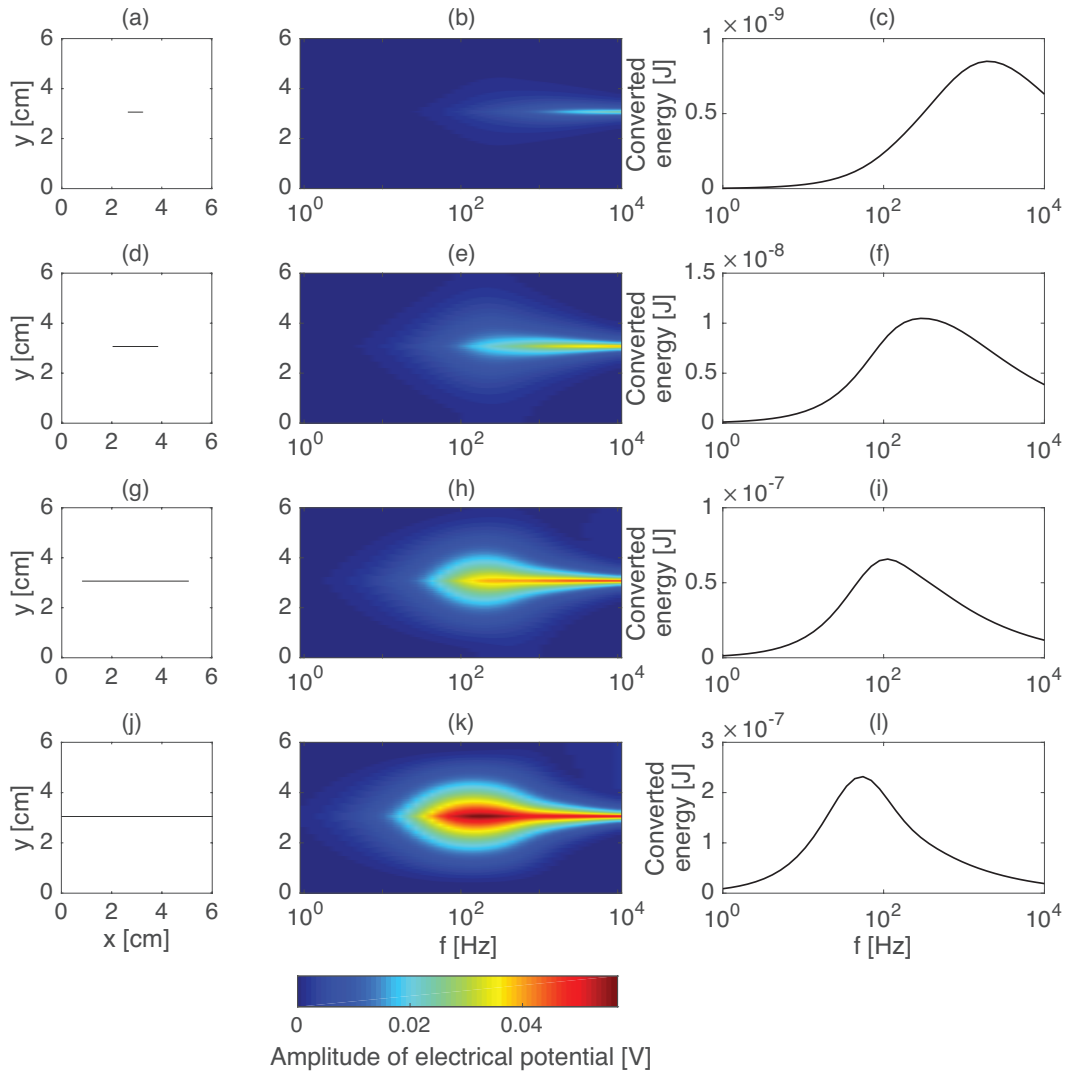
826 **Figure 6.** Seismoelectric dependence on pore water electrical conductivity. Amplitude of the electrical
 827 potential along the y -axis as a function of frequency for the same sample as shown in Fig. 5a but considering
 828 a pore water salinity that is (a) one order-of-magnitude smaller ($\sigma^f = 0.001 \text{ S m}^{-1}$) and (b) one order-of-
 829 magnitude larger ($\sigma^f = 0.1 \text{ S m}^{-1}$). Given the large amplitude difference, we use separate color scales for
 830 each subplot.



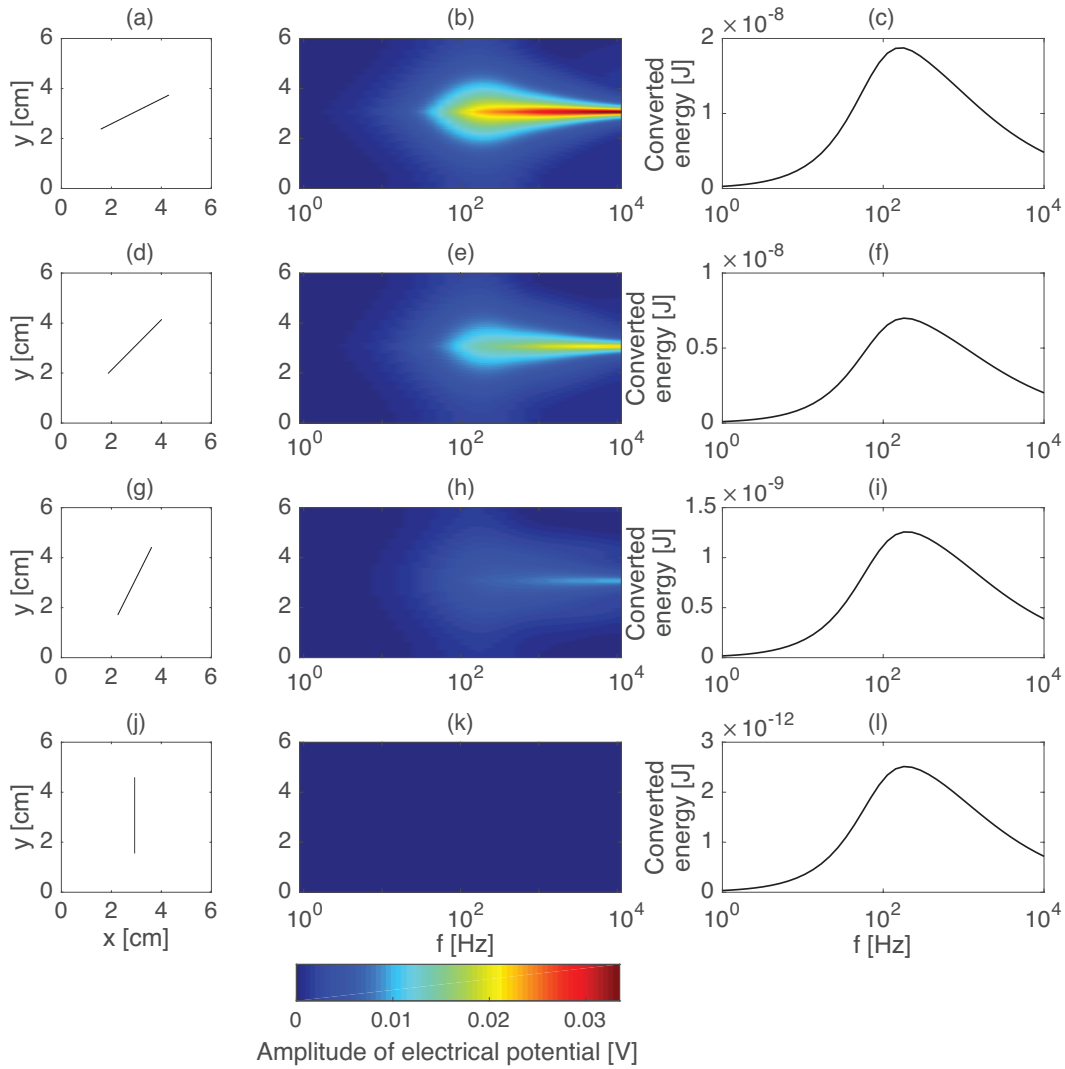
831 **Figure 7.** (a) Synthetic rock sample used as the basis to study the seismoelectric dependence on the proper-
 832 ties of fractured media. A single horizontal fracture is embedded in an otherwise homogeneous medium. The
 833 sensitivity analysis presented in the following is based on simple variations of this initial model. (b) Ampli-
 834 tude of the electrical potential generated for a frequency of 142 Hz with a virtual reference electrode located
 835 at the left bottom edge of the sample. The amplitude of the stress applied on the top boundary of the sample
 836 ΔP is 1 kPa.



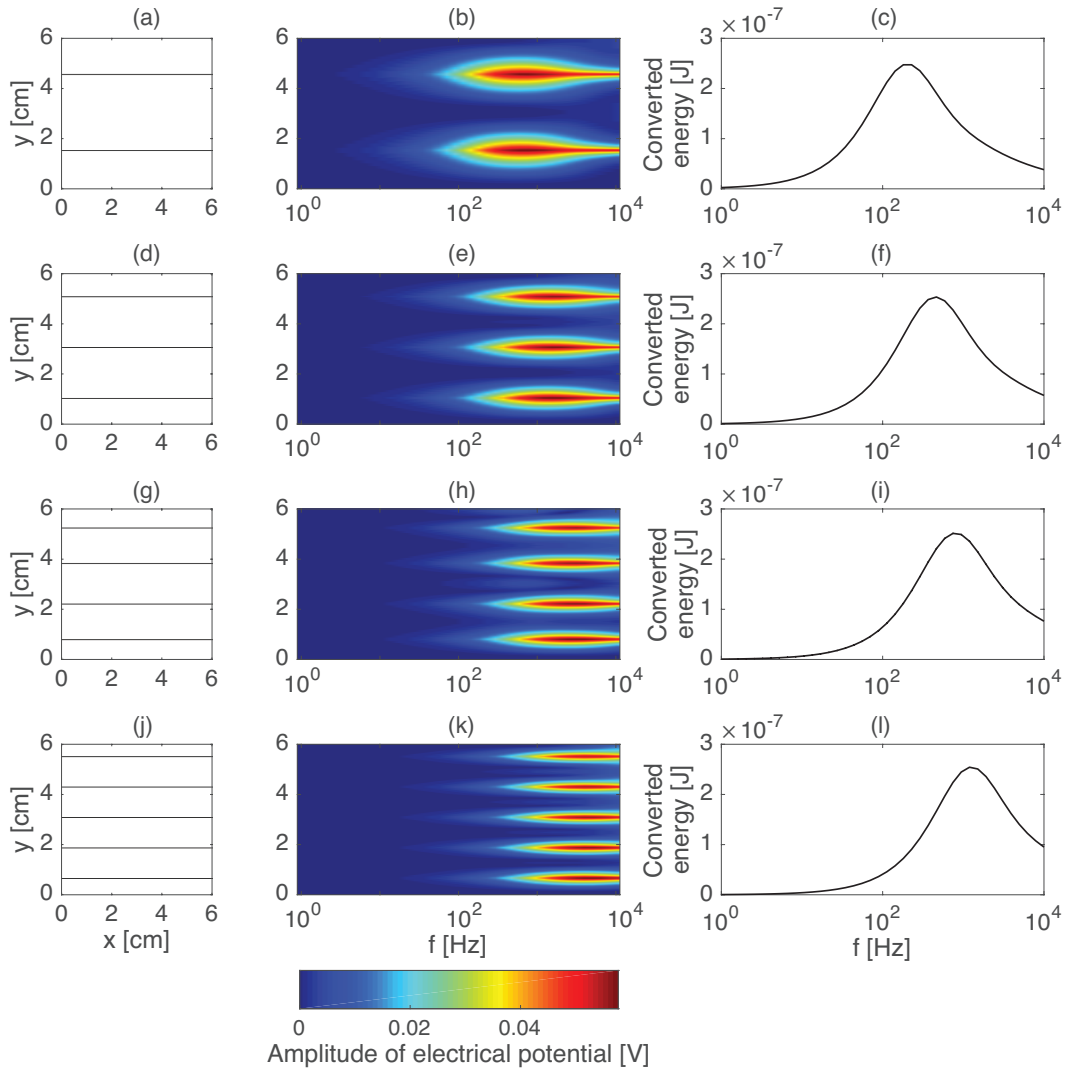
837 **Figure 8.** Vertical cuts of the electrical potential at the center ($x = 3$ cm) of the sample shown in Fig. 7a as
 838 a function of frequency. (a) Amplitude and (b) total energy converted to seismoelectric signal in one cycle as
 839 a function of frequency.



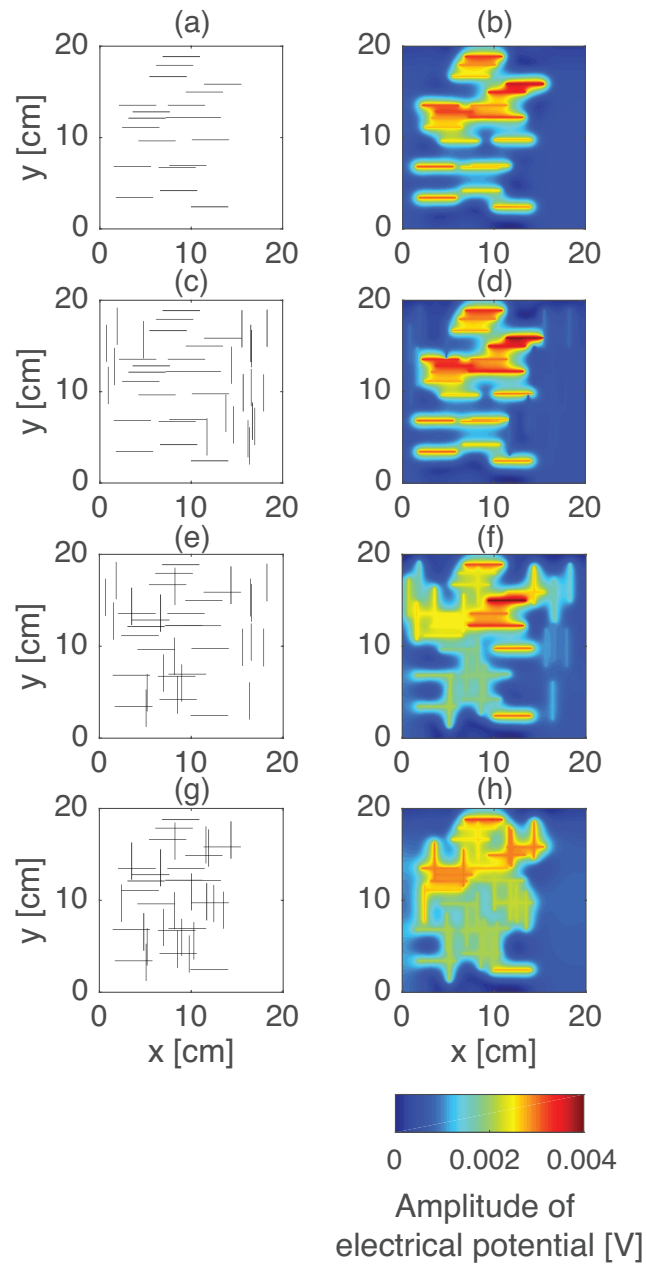
840 **Figure 9.** Dependence of seismoelectric signals on fracture length. (a), (d), (g) and (j) Samples with the
841 same properties as Fig.7a but with different fracture lengths. (b), (e), (h) and (k) Vertical cuts of the amplitude
842 of the electrical potential at the center ($x = 3$ cm) of the corresponding samples as functions of frequency. (c),
843 (f), (i) and (l) Total converted electrical energy as a function of frequency.



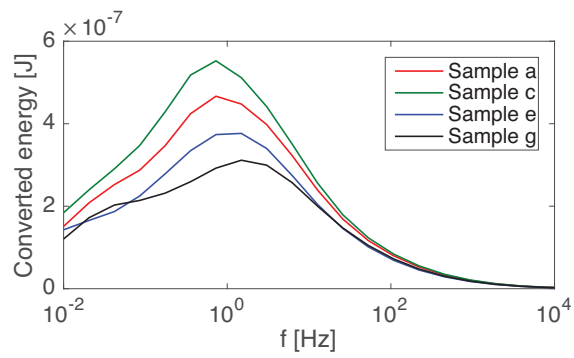
844 **Figure 10.** Dependence of seismoelectric signal on fracture orientation. (a), (d), (g) and (j) Samples with
845 the same properties as Fig. 7a but with different fracture orientation, ranging from sub-horizontal to vertical.
846 The angles with respect to the x -axis are: (a) 27° , (d) 45° , (g) 67.5° and (j) 90° . (b), (e), (h) and (k) Verti-
847 cal cuts of the amplitude of the electrical potential at the center ($x = 3$ cm) of the corresponding samples as
848 functions of frequency. (c), (f), (i) and (l) Total converted electrical energy as a function of frequency.



849 **Figure 11.** Dependence of seismoelectric signal on fracture density. (a), (d), (g) and (j) Samples with
 850 the same properties as Fig.7a but with different number of fractures. (b), (e), (h) and (k) Vertical cuts of the
 851 amplitude of the electrical potential at the center ($x = 3$ cm) of the corresponding samples as functions of
 852 frequency. (c), (f), (i) and (l) Total converted electrical energy as a function of frequency.



853 **Figure 12.** Left column: Rock samples used to test the effect of fracture connectivity on the seismoelectric
 854 signal. (a) Sample containing horizontal fractures that are not connected between each other. (c) Sample con-
 855 taining the same horizontal fractures as (a), plus vertical fractures, which are not connected to the horizontal
 856 ones. (e) Sample containing the same amount of horizontal and vertical fractures as in (c) but with some of
 857 the fractures connected. (g) Same as (b) but with most of the fractures connected. Right column: Amplitudes
 858 of the electrical potential in the samples shown in the left column for a frequency of 0.73 Hz.



859 **Figure 13.** Total energy converted to seismoelectric signal in one period as a function of frequency for the
 860 samples shown in Fig. 12a, c, e, and g.